ADVANCED ENERGY MATERIALS
www.advenergymat.de

Hole Transporting Bilayers for Efficient Micrometer-Thick Perovskite Solar Cells

*Yueming Wang, Samah Akel, Benjamin Klingebiel, and Thomas Kirchartz**

Achieving high efficiencies in halide perovskite solar cells with thicknesses >1 µm is necessary for developing perovskite-Si tandem cells based on small pyramidal structures. To achieve this goal, not only is the perovskite layer quality to be optimized but also the properties of the charge-transport layers must be tuned to reduce charge-collection losses. The transport layers provide a non-ohmic resistance that modulates the Fermi-level splitting inside the perovskite absorber. The finite conductivity of the transport layers can lead to losses in the fill factor (*FF*) and short-circuit current, even at infinite charge-carrier mobility in the absorber layer. These losses notably scale with the absorber layer thickness, which implies that higher-conductivity transport layers are required for thicker perovskite absorbers. One strategy to improve charge collection and thereby *FF*s in thick inverted perovskite solar cells is to use bilayers of hole-transport layers. In this study, the combination of poly[bis(4-phenyl) (2,4,6-trimethylphenyl)amine] with self-assembled monolayers provides the best photovoltaic performance in single-junction devices.

1. Introduction

Lead-halide perovskite solar cells have attracted considerable research interest in the photovoltaic field owing to their exceptional performance and cost-effective fabrication processes.[1,2] Single-junction perovskite solar cells have achieved certified power-conversion efficiencies of more than 25%.[3,4] However, the efficiency of single-junction cells is fundamentally limited to ≈33%,[5,6] whereas tandem solar cells could, in principle, approach efficiencies of 45% by reducing thermalization and transmission losses.[7,8] The tunable band gap and high efficiency at relevant band gaps in the 1.6 to 1.7 eV range make lead-halide perovskites attractive candidates for tandem solar cells. However, the most popular candidate as a low-bandgap partner for halide perovskites is the indirect bandgap semiconductor silicon, which requires surface texturing to achieve a sufficiently sharp absorption onset.[9] While earlier efforts to deposit perovskite top cells onto double-side textured silicon bottom cells focused on the conformal coverage of large pyramids using methods involving the evaporation of lead-halogenides,[10] more recent approaches[11] have been based on covering smaller pyramids with solution-processing methods.

To completely cover smaller pyramids with a pinhole-free perovskite film, the film must be sufficiently thick (typically thicker than 1 µm). As most high-efficiency perovskite solar cells have typical thicknesses in the 400–800 nm range,[1,12,13] the optimization of such thicker perovskite solar cells requires optimization strategies that are different from those used in the bulk of the perovskite solar cell literature. Further increasing the thickness typically reduces the open-circuit voltage V_{oc} and fill factor *FF*[14,15] implying that special strategies must be developed to keep these parameters as high as possible when increasing the thickness. The thickness-dependent loss in open-circuit voltage is due to a sub-linear increase of the generation rate with thickness, which in consequence reduces the carrier density at which generation and recombination are equal at larger thicknesses.[16,17] The thickness-dependent fill-factor losses can have both fundamental[18] and processing-specific reasons. They are often attributed to a reduced level of control over the crystallization process, poor surface morphology,[19] increased defect density,[20] and deterioration of charge extraction.[21] Efforts dedicated to improving the device performance of perovskite solar cells with >1 µm thickness were therefore focused on defect passivation,[22] gaining better control over the crystallization process,[23] absorber-layer doping using molecules, such as F6TCNNQ,[24] self-limiting molecules for perovskite film surface post-treatment,[11] and charge-transport layer optimization.[25–27] Through these strategies, the *FF* can reach values of ≈80% with high efficiencies. However, as shown in **Figure 1**a and Figure S1, Supporting Information, most reports on thick films employ perovskite compositions with band gaps lower than 1.65

Y. Wang, S. Akel, B. Klingebiel, T. Kirchartz
IEK5-Photovoltaik
Forschungszentrum Jülich
52425 Jülich, Germany
E-mail: t.kirchartz@fz-juelich.de
T. Kirchartz
Faculty of Engineering and CENIDE
University of Duisburg-Essen
Carl-Benz-Str. 199, 47057 Duisburg, Germany

The ORCID identification number(s) for the author(s) of this article can be found under https://doi.org/10.1002/aenm.202302614

DOI: 10.1002/aenm.202302614

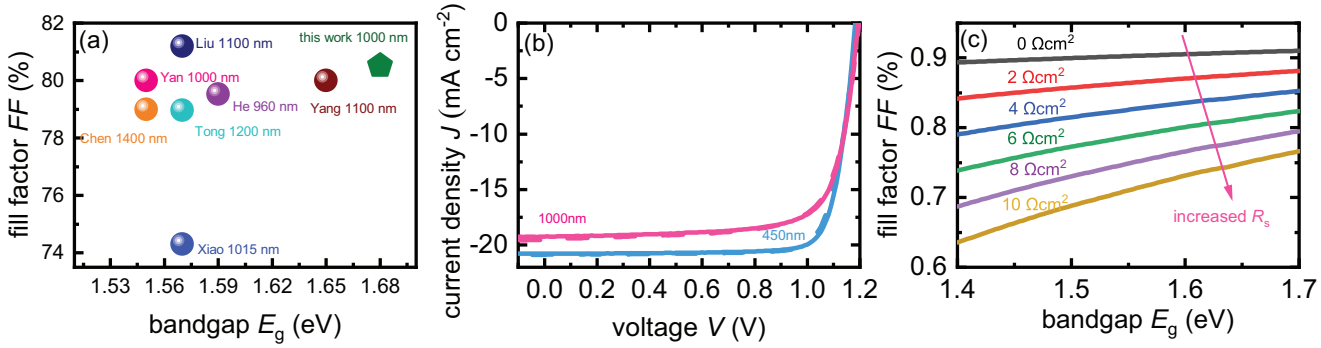

Figure 1. a) Comparison of the *FF* and the corresponding perovskite film thickness and bandgap in the representative reports and this work. b) Illuminated *J*–*V* curves of perovskite solar cells with different thicknesses based on Me-4PACz, the cell performance parameters are listed in Table S1, Supporting Information. c) Fill factor as a function of the bandgap according to Equation (1) considering different resistances.

eV[20,22,23,25–28] which are not ideally suited for monofacial[29] two-terminal tandem applications with Si bottom cells.

Here, we report a method to fabricate over 1-micrometer thick perovskite by employing hole-transporting bilayers of self-assembled monolayers (SAMs) and poly[bis(4-phenyl) (2,4,6-trimethylphenyl)amine] (PTAA). The 1.68 eV band gap, opaque perovskite solar cells reach efficiencies above 20% with *FF*s over 80%, which presents a comparably high performance among the over 1-micrometer thick film solar cells shown in Figure 1a and Figure S1, Supporting Information. The peculiar finding of this study is that it is primarily the modification of charge-transport layers that can provide leverage to improve the fill factor of thick perovskite solar cells. Furthermore, the losses associated with the transport layers are not purely resistive. Instead, the finite mobilities of the charge carriers in the transport layers modulate the carrier concentration in the absorber layer as long as a finite current is extracted. Thereby, the recombination losses at short circuit or the maximum power point (MPP) depend not only on the mobility-lifetime product of the absorber and the interface recombination velocity[30] but also critically on the properties of the transport layers.[31,32] Furthermore, for thicker absorber layers, the mobility in the transport layer must increase proportionally with the thickness increase to achieve the same efficiency of charge-carrier collection. This is a somewhat counterintuitive finding as it explains thickness-dependent performance deterioration that is independent of traditional explanations for the thickness dependence of the charge-collection efficiency that is based on the diffusion- or drift-length of the absorber.[33,34]

2. Results

Different hole-transport layers, PTAA and phosphonic acid-functionalized carbazole-based SAMs, such as Me-4PACz ([4-(3,6-dimethyl-9H-carbazol-9-yl)butyl]phosphonic acid) and MeO-2PACz ([2-(3,6-dimethoxy-9H-carbazol-9-yl)ethyl]phosphonic acid), were employed to investigate their influence on micrometer-thick perovskite solar cells. The perovskite films were deposited by a one-step spin-coating method using an anti-solvent. The structure of the inverted planar perovskite solar cell is ITO/hole-transport layer/perovskite/C_{60}/BCP/Ag. An organic halide salt 4-fluorophenethyl-ammonium iodide (F-PEAI) was added to the perovskite precursor solution for defect passivation. The optimized concentration of F-PEAI is shown in Figure S2, Supporting Information.

2.1. Micrometer-Thick Perovskite Solar Cell Fabrication

We focused on the triple-cation perovskite $Cs_{0.05}FA_{0.8}MA_{0.15}PbI_{2.25}Br_{0.75}$, because of its suitable bandgap for the top cells of the perovskite-Si tandem. Me-4PACz was used as the hole transport layer. 1.4 M precursor solution was spin-coated on the substrates to obtain perovskite thin films, and an efficiency of 20.02% was achieved (shown in Figure S3c, Supporting Information). To increase the thickness of the perovskite films to one micrometer, the precursor solution concentration was increased up to 1.7 M combined with a reduced spin-coating speed.[19] Scanning electron microscopy (SEM) images revealed high roughness and wrinkles (Figure S4c, Supporting Information) in a nearly 1.2 µm thick perovskite film (Figure S5, Supporting Information). The thick-film perovskite solar cells suffer from reduced performance compared to the thin-film cells. In particular, the short-circuit current J_{sc} and the *FF* were reduced when the absorber thickness was increased (Figure 1b and Figure S3c,d, Supporting Information). The increased series resistance (R_s) is a major limitation for fabricating thick-film perovskite solar cells with high efficiencies (Figure S3, Supporting Information). The efficiency loss $\Delta\eta_{Rs}$ due to the series resistance for thin-film perovskite solar cells is 1.73%, while the $\Delta\eta_{Rs}$ for thick-film perovskite solar cells increased to 3.17% (parameters listed in Table S2, Supporting Information).

2.2. Micrometer-Thick Perovskite Solar Cells Based on Different Hole Transport Layers

The *FF* of thick-film perovskite solar cells increased by spin coating a thin layer of PTAA on top of Me-4PACz (Figure S6, Supporting Information). The dependence of the device performance on the PTAA solution concentration from 0.5 to 2 mg mL^{-1} is shown in Figure S6, Supporting Information. The optimal performance was obtained at a concentration of 0.5 mg mL^{-1}. The device based on Me-4PACz covered by PTAA can reach an *FF* over 77%, which is, however, still insufficient to compete with state-of-the-art *FF*

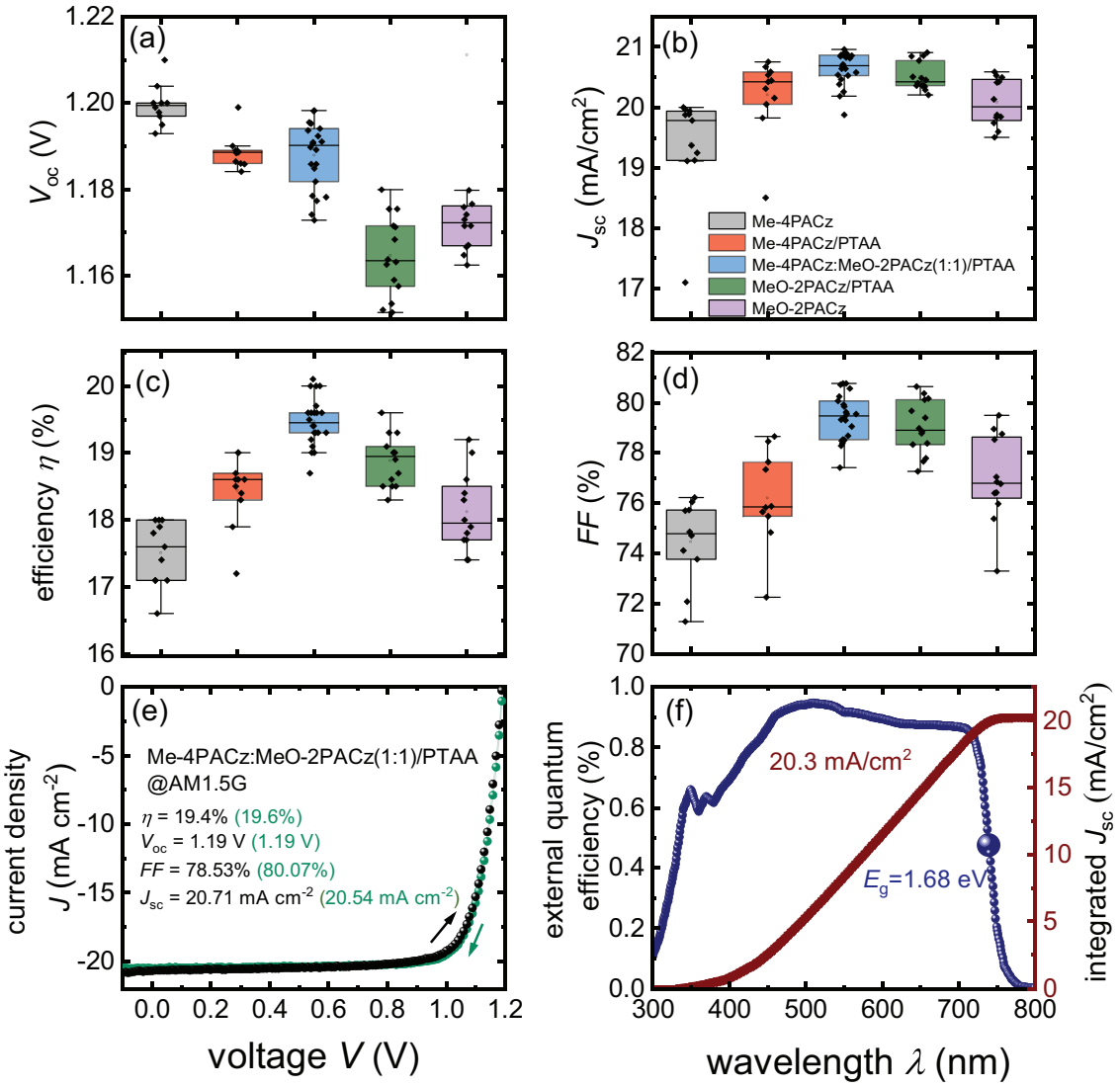

Figure 2. The statistics of a) open-circuit voltage V_{oc}, b) short-circuit current J_{sc}, c) efficiency, and d) fill factor *FF* for the different hole transport layers studied. e) Illuminated current–voltage curve of a 1 µm thick perovskite solar cell with Me-4PACz: MeO-2PACz (1:1)/PTAA measured with a sun simulator in forward and backward scan directions. f) External quantum efficiency (EQE) spectrum and integrated J_{sc} for perovskite solar cells with a structure the same as the one shown in (e).

values. As for MeO-2PACz with PTAA in the optimized conditions, the *FF* approaches nearly 80% but the open-circuit voltage V_{oc} is significantly reduced to around 1.16 V. The current density-voltage (*J*–*V*) curves and the external quantum efficiency (EQE) spectrum of over 1-micrometer thick perovskite solar cells based on Me-4PACz, Me-4PACz/PTAA, MeO-2PACz, and MeO-2PACz/PTAA are shown in Figure S7, Supporting Information.

Me-4PACz and MeO-2PACz were mixed and then covered by PTAA to function as a hole transport layer for micrometer-thick wide-bandgap perovskite solar cells. Solar cells based on a mixture of SAMs with PTAA show significantly higher average *FF* and efficiency than those based on a single type of SAM or a single type of SAM with PTAA (**Figure 2**a–d). Figure 2e shows the *J*–*V* curve of a Me-4PACz: MeO-2PACz (1:1)/PTAA device measured using a class AAA solar simulator under forward and reverse scan conditions. An efficiency of 19.6% was achieved owing to the high *FF* of 80.07% and the short-circuit current density J_{sc} of 20.54 mA cm^{-2} and V_{oc} of 1.1937 V shown in Figure 2e. A 300 s MPP tracking is shown in Figure S8, Supporting Information. The bandgap E_g of the perovskite of 1.68 eV is obtained from the EQE spectrum presented in Figure 2f. The resulting integrated J_{sc} is in close agreement with the values from the *J*–*V* curves.

We used different molar ratios of the Me-4PACz/MeO-2PACz mixture as a hole-transport material to determine the optimal ratio for maximizing the performance of thick perovskite solar cells. As shown in Figures S9 and S10, Supporting Information, both the mixture of Me-4PACz to MeO-2PACz (3:1) and a mixture of Me-4PACz to MeO-2PACz (1:3) exhibit a solar cell efficiency near 20% and *FF* over 80%. Since the different ratios of mixture SAMs covered by PTAA show small differences in device performance, the ratio of Me-4PACz to MeO-2PACz (1:1) was chosen for further characterization.

2.3. Fill-Factor Losses

As shown in Figure 1b, the fill factor losses are one of the main limitations of high-efficiency thick-film perovskite solar cells. In the limit of infinitely large parallel resistances, the fill factor approximately follows the relation[35]

$$FF = \frac{v_{oc} - \ln\left(v_{oc} + 0.72\right)}{v_{oc} + 1}\left(1 - R_s \frac{J_{sc}}{V_{oc}}\right) \tag{1}$$

The normalized open-circuit voltage is defined as $v_{oc} = qV_{oc}/n_{id}k_BT$, with k_B being the Boltzmann constant, q the elementary charge, T the temperature of the solar cell, and n_{id} the ideality factor. Equation (1) is a simplified relation that is based on the one-diode model of solar cells with a perfectly ohmic series resistance. Figure 1c shows the relation of FF as a function of bandgap and series resistance in a solar cell that is—except for its finite series resistance—consistent with the Shockley–Queisser model. The small dependence of FF on the band gap is mainly caused by the differences in the photocurrent causing different degrees of voltage losses over the series resistance.

In real solar cells, many physical effects contribute to resistive effects that are in series with the diode and current source that constitute the equivalent circuit of an ideal solar cell. The contributions to the series resistance may originate from the lateral current transport in the ITO or Ag electrodes but also from the resistive effects of charge-transport layers and the perovskite absorber itself. The latter contributions to R_s are non-ohmic as they result from the finite conductivity of intrinsic or weakly doped semiconductors that depends critically on the optically or electrically injected charge density. The common feature of series resistance losses is that they increase with increasing current flow through the diode, and hence, matter at higher currents (and voltages).

In addition to series resistances, parallel resistances can further reduce the FF of solar cells. In many solar cells, however, the parallel resistance in the dark is so high that it does not matter for the one-sun operation of a solar cell. However, solar cells typically exhibit a shunt-like behavior[31,36–40] under illumination that is significantly different in origin and magnitude from the behavior in the dark. This phenomenon is sometimes called a photoshunt and originates from ohmic-looking recombination currents; that is, recombination currents that still depend exponentially on the quasi-Fermi level splitting but linearly on the external voltage.[40,41] Due to their linear dependence on the external voltage, they appear phenomenologically like a shunt. Finally, the FF is also reduced by ideality factors that increase above unity as seen in Equation (1). This loss in fill factor is a consequence of recombination mechanisms that change exponentially with voltage but scale differently than with $\exp(qV/kT)$.

To quantify and analyze fill factor losses, a sensible first step is to determine the series resistance keeping in mind that it will not be a scalar value but a function of voltage and current. A convenient approach to determine a voltage-dependent series resistance is based on the comparison between the current–voltage curves under illumination and in the dark.[42–44] The current–voltage curve of a solar cell under illumination that is affected by R_s but not R_p is written as

$$J_l = J_0\left(\exp\left(\frac{q\left(V_l - J_l R_s\right)}{n_{id}kT}\right) - 1\right) - J_{sc} \tag{2}$$

where J_0 is the saturation current density of the solar cell. The current–voltage curve in the dark is written in the same logic as before as

$$J_d = J_0\left(\exp\left(\frac{q\left(V_d - J_d R_s\right)}{n_{id}kT}\right) - 1\right) \tag{3}$$

The main differences between Equations (2) and (3) are the J_{sc} that is missing in the dark and the different terms for the voltage drop over the series resistance. If one shifts the dark and light J–V curves into the same quadrant (both then being either in the first or fourth quadrant), they will be horizontally offset by a term that scales with the series resistance. The easiest way to understand this phenomenon is to compare the situation, where the recombination currents are equal to J_{sc}. Under illumination, at a recombination current of J_{sc}, the total current is zero (recombination balanced by generation), and the voltage drop over any series resistance vanishes. In the dark, however, the voltage drop is $J_d R_s = J_{sc} R_s$. Thus, the series resistance R_s can be determined from the difference between V_l and V_d at a constant recombination current via[45]

$$R_s = \left(V_d - V_l\right)/J_{sc} \tag{4}$$

Figure 3a,b shows the dark current–voltage curve JV_d and illuminated current–voltage curve JV_l shifted by the short circuit current J_{sc} in the first quadrant using a logarithmic current axis for cells with different hole transport layers. On a logarithmic scale, the shifted illuminated current–voltage curve shows a moderate slope in the low-voltage region. This feature is referred to as photoshunt, which indicates poor carrier extraction at low voltages.[40] In Figure 3a,b, Me-4PACz has the highest photoshunt conductance (the lowest shunt resistance), whereas the Mixed SAMs/PTAA-bilayer shows the lowest shunt conductance (highest shunt resistance). The SAM/PTAA bilayer has a lower photoshunt conductance than the SAMs without PTAA. This is consistent with a better FF and J_{sc} by covering PTAA on SAMs shown in Figure 2b,d.

As shown in Figure 3c, the R_s of solar cells for different hole transport layers calculated from Equation (4) increases when the voltage is reduced because of the increasing internal resistance in the solar cells. When the voltage increases, the R_s saturates. For a clear comparison, the R_s at 1.18 V cells for different hole transport layers is shown in **Figure 4d**. The Me-4PACz has the highest R_s of 16.46 Ω cm^2 while the Mixed SAMs/PTAA-bilayer has the lowest R_s of 1.09 Ω cm^2. The value of R_s is consistent with the FF distribution of different hole transport layer devices (Figure 2d). The cells of the SAM mixture/PTAA with the lowest R_s perform the best efficiency of 19.6% and FF of 80.07% (Figure 2e).

The ideality factor n_{id} is also an important parameter influencing the FF. The n_{id} was determined by $J_{sc}V_{oc}$ measurements as a

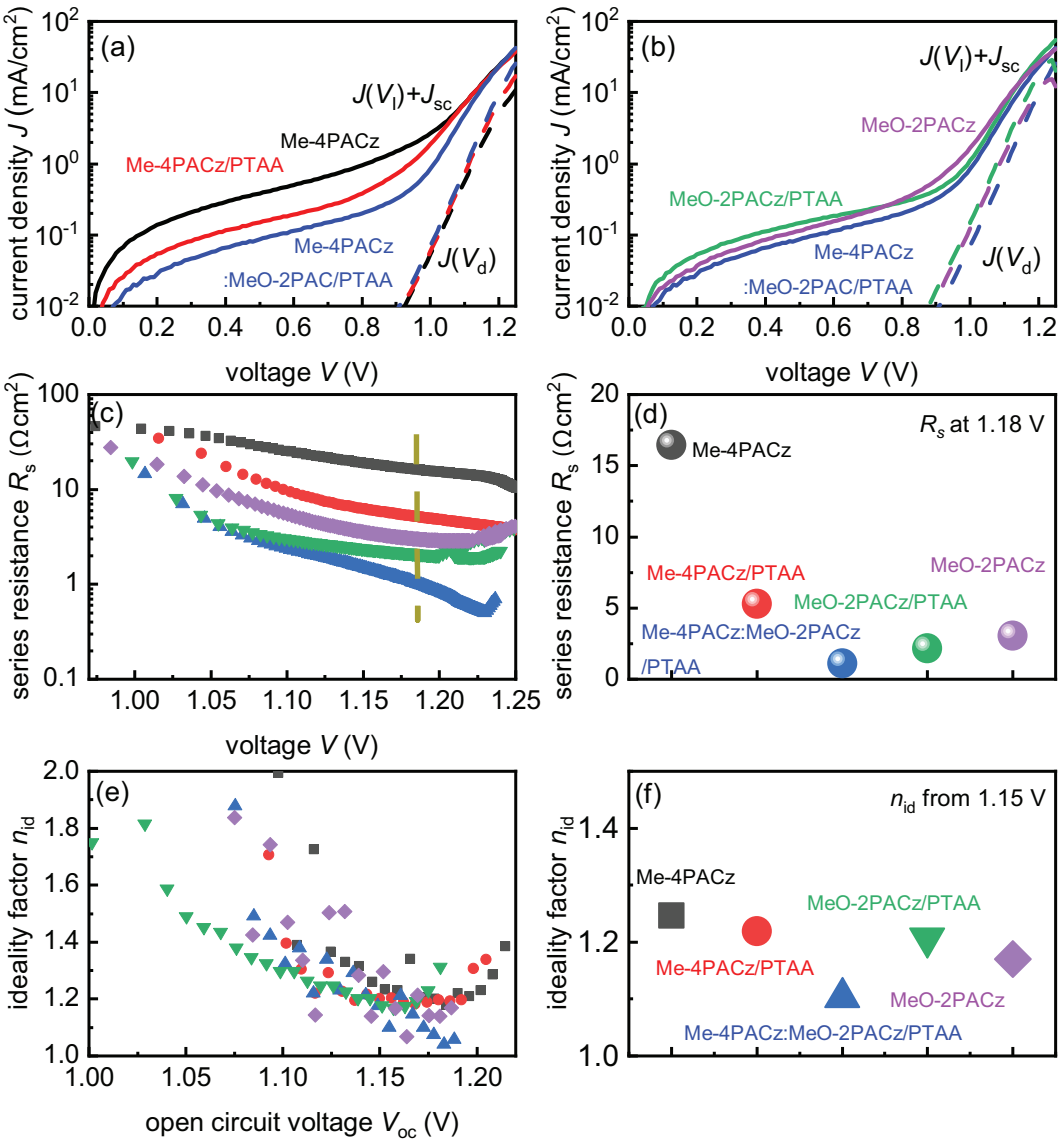

Figure 3. a,b) Dark (dashed line) and illuminated (solid line) *J–V* curve of the different hole transport layers plotted in the first quadrant. c) Series resistance calculated from the difference between the dark and illuminated *J–V* curve. d) Comparison of series resistance at a voltage of 1.18 V. e) Ideality factor n_{id} derived from the Suns-V_{oc} measurement. f) Comparison of the average ideality factor n_{id} calculated from 1.15 V.

function of light intensity. The relation between J_{sc} and V_{oc} can be approximately expressed as

$$J_{sc} = J_0 \left(\exp\left(\frac{qV_{oc}}{n_{id}kT} \right) - 1 \right) \tag{5}$$

which implies that the ideality factor follows from $n_{id} = qdV_{oc}/[kTd\ln(J_{sc})]$. The voltage-dependent n_{id} values of solar cells with different hole transport layers are shown in Figure 3e. The average value of n_{id} calculated from the voltage of 1.15 V to the end of the measurement can be seen in Figure 3f. The n_{id} of different hole transport layers ranges from 1.1 to 1.25. All values are much lower than 2 and do not exhibit large differences, suggesting that the limiting recombination mechanism does not occur via deep defects. The *FF* losses due to the nonideal n_{id} (ΔFF_{nid}) determined from Equation (6) and listed in **Table 1** for the solar cells with different hole transport layers are ≈2%. Therefore, the main factor influencing the *FF* in a thick perovskite solar cell is the voltage-dependent series resistance.

$$\Delta FF_{n_{id}} = FF_{id} - FF_{J_{sc}V_{oc}} \tag{6}$$

Equation (5) also provides the current–voltage curve of a solar cell that does not involve a series resistance. To investigate the *FF* losses due to the series resistance, the power densities derived from the $J_{sc}V_{oc}$ curves and the JV_I curve are plotted in Figures S11 and S12, Supporting Information. The difference in *FF*

Table 1. *FF* and efficiencies η for solar cells based on different hole transport layers compared to *FF* and η from an ideal *J–V* curve with the same J_{sc} and V_{oc} but $R_s = 0$ and $n_{id} = 1$ and a curve with zero series resistance (but nonideal n_{id}), derived from the measurement of the J_{sc}/V_{oc} curves shown in Figure S12, Supporting Information.

	FF_I	FF_{JscVoc}	FF_{id}	η	η_{JscVoc}	η_{id}	ΔFF_{R_s}	$\Delta FF_{n_{id}}$
Me-4PACz	73.02%	87.66%	89.7%	16.54%	20.2%	20.3%	14.64%	2.04%
Me-4PACz /PTAA	76.43%	87.66%	89.65%	18.45%	21.3%	21.65%	11.23%	1.99%
SAM mixture /PTAA	80.76%	87.59%	89.87%	20.2%	22%	22.48%	6.83%	2.28%
MeO-2PACz /PTAA	80.98%	87.37%	89.61%	19.75%	21.34%	21.85%	6.39%	2.24%
MeO-2PACz	78.11%	87.73%	89.79%	19.14%	21.22%	21.95%	9.62%	2.06%

obtained from the two curves reveals the loss because of the series resistance ΔFF_{R_s} and follows from

$$\Delta FF_{R_s} = FF_{J_{sc}V_{oc}} - FF_I \quad (7)$$

The ΔFF_{R_s} of the Me-4PACz-based solar cell is 14.64%, whereas the ΔFF_{R_s} values of samples with the mixed-SAMs/PTAA HTL, as well as the MeO-2PACz/PTAA HTL, decreased to significantly lower values of 6.83% and 6.39%, respectively (listed in Table 1).

2.4. Energy-Level Alignment

The interfaces between the absorber layer and the transport layers have a strong influence on charge extraction and recombination in perovskite solar cells. Therefore, the energy-level alignment of the different layers considerably affects device performance. Ultraviolet photoelectron spectroscopy (UPS) measurements were conducted to investigate the energy-level alignment of the different hole-transport layers mentioned above and the perovskite film. The UPS data analysis is shown in Figures S13–S15, Supporting Information. As shown in Figure 4, the valence-band maximum (VBM) and Fermi energy E_F can be determined relative to the vacuum energy $E_{vac} = 0$ eV by UPS. We used literature values for the pure SAMs and PTAA, E_g (PTAA) = 3.4 eV, E_g (Me-4PACz) = 3.3 eV, and E_g (MeO-2PACz) = 3.2 eV and assumed that E_g (SAMs/PTAA) of the combined SAMs and PTAA equals that of pure PTAA as this is much thicker.[46] The E_g of the perovskite film of 1.68 eV was obtained from the inflection point of the EQE spectrum. The distance from the conduction band minimum (CBM) to the vacuum energy can be calculated from the VBM and bandgap of each layer.

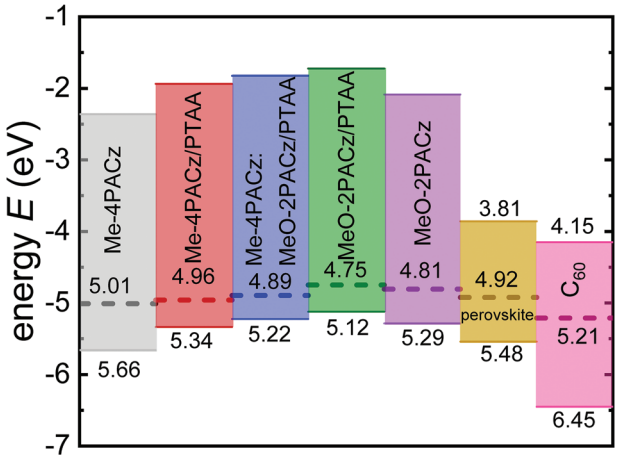

Figure 4. Schematic of the energy levels for different hole-transport layers, perovskite, and C_{60} deposited on top of the perovskite. We note that the Me-4PACz generally leads to lower-lying HOMO levels of the hole-transport materials as compared to MeO-2PACz. The addition of PTAA further reduces the effective ionization potential of the hole-transport layers.

The distance from E_F to VBM is 0.65 eV in Me-4PACz, and this value decreases to 0.38 eV by covering PTAA on top of Me-4PACz. MeO-2PACz/PTAA shows a shorter distance from E_F to the VBM (0.38 eV) than MeO-2PACz (0.48 eV). The mixed SAMs/PTAA bilayer has a lower value of $E_F - E_V = 0.33$ eV than every single type of SAM/PTAA. The SAMs/PTAA bilayer shows a stronger p-type character than the SAMs without PTAA in the energy level diagram.[47] As for the hole transport layers, the ionization potential E_i, which is determined as the distance from VBM to vacuum energy, is an important parameter for hole collection and interface recombination. Me-4PACz shows the highest E_i of 5.66 eV and the closest alignment to the VBM of perovskite, which agrees well with the V_{oc} shown in Figure 2a. The Me-4PACz/PTAA exhibits a lower E_i of 5.34 eV and a stronger band gap offset than Me-4PACz. MeO-2PACz/PTAA shows the lowest E_i of 5.12 eV and the highest band gap offset.

2.5. Transient Photoluminescence

Interface recombination is central to the understanding of V_{oc} losses in solar cells. The energy-level alignment, as well as the recombination velocity between perovskite and charge-transport layers, can influence the interface recombination.[48] Transient photoluminescence (PL) has frequently been used to analyze the charge-carrier dynamics of full devices, layer stacks, and films.[49–51] While the measurement is relatively simple and applicable to layer stacks (no devices needed), the interpretation of the data is often complicated—especially in situations where the decay is not exponential throughout the investigated range of carrier densities. Here, we use transient photoluminescence to study the recombination dynamics at perovskite-HTL interfaces and attempt to interpret the peculiar carrier-density dependence of the data.

The normalized time-resolved photoluminescence (tr-PL) decays measured on samples of layer stacks with an ITO/hole

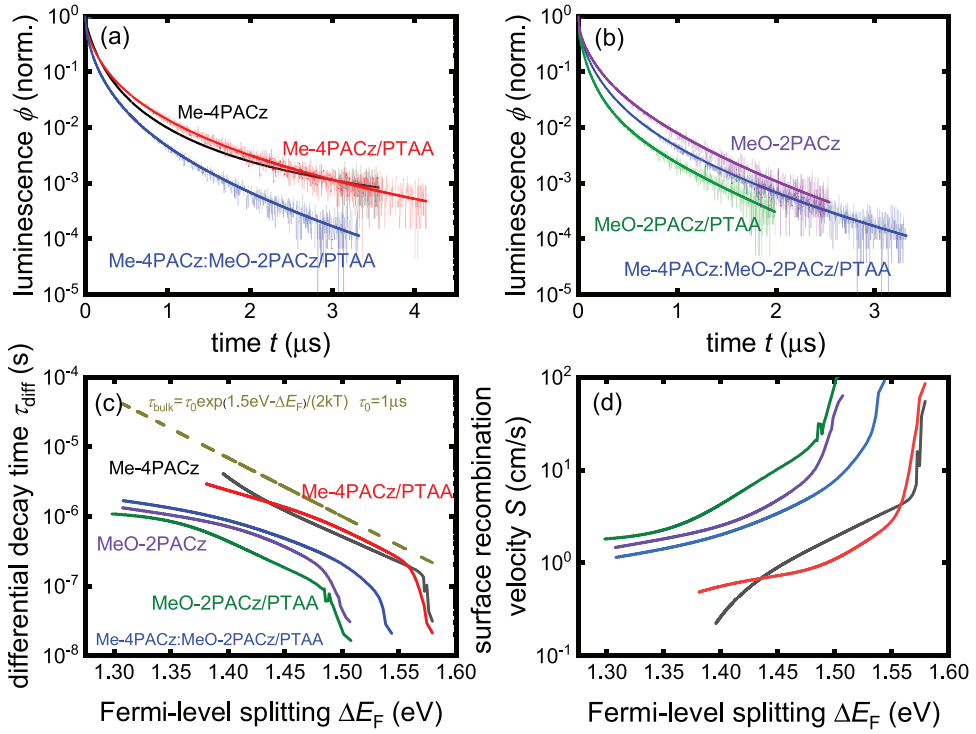

Figure 5. a,b) Normalized transient photoluminescence of glass/ITO/hole transport layer/perovskite measured with time-correlated single photon counting (TCSPC). The normalized data were fitted with rational functions (darker lines). c) The differential decay time calculated from fitted normalized transient photoluminescence (solid lines) and τ_{bulk} (dashed line) plotted versus Fermi-level splitting. d) Surface-recombination velocity S estimated with Equation (9).

transport layer/perovskite structure are shown in **Figure** 5a,b. To analyze the differential decay time τ_{diff}, we use the relation[52]

$$\tau_{diff} = -2\left(\frac{d\ln(\phi)}{dt}\right)^{-1} \quad (8)$$

where ϕ is the intensity of luminescence and the factor 2 represents the expectation that lead-halide perovskites are typically undoped,[53] that is, $\phi \propto n^2$. The differential decay time τ_{diff} as a function of the quasi-Fermi level splitting ΔE_F is plotted in Figure 5c. ΔE_F is proportional to $\ln(\phi)$ + const, whereby a higher ΔE_F corresponds to earlier times after the laser pulse. The short differential decay times of different samples at high quasi-Fermi level splitting imply a fast initial decay of the photoluminescence. At early times after the pulse, radiative and Auger recombination or charge transport to the hole transport layer and ITO electrode affect the differential decay time. At lower quasi-Fermi level splitting, which corresponds to later times after the laser pulse, the differential decay times continuously increase. While there are only minor differences in the slope of the decay time versus Fermi-level splitting, the samples show differences in the absolute value at a given Fermi-level splitting. The values of the τ_{diff} at $\Delta E_F = 1.45$ eV are summarized in Figure S16, Supporting Information. Me-4PACz showed the longest decay time of 4.1 μs, while the Me-4PACz/PTAA showed a shorter decay time of 2.9 μs compared with Me-4PACz. Similarly, MeO-2PACz/PTAA exhibited a shorter differential decay time than MeO-2PACz. The τ_{diff} obtained from different laser intensities are plotted in Figure S17, Supporting Information. The differential decay time reveals that the SAM/PTAA bilayers lead to more nonradiative recombination than the SAMs. Me-4PACz: MeO2-PACz (1:1)/PTAA showed an intermediate differential decay time among the five different hole transport layers.

The most frequently used approach to determine surface-recombination velocities is to assume that the total recombination rate is given by a sum of the bulk and surface recombination rates, which is a good assumption for flat Fermi levels. If the rates are additive terms, the inverse lifetimes for bulk and surface would add up to the inverse measured lifetime of the bilayer. Therefore, a reasonable bulk lifetime must be assumed or measured. As we have recently shown[54,55] bulk lifetimes in halide perovskite films are often a strong function of carrier density or Fermi-level splitting, we can only apply the above approach if we consider all lifetimes and recombination velocities to be a function of ΔE_F. The physical reason for this necessity is that, in the presence of a significant density of shallow traps, the SRH formalism predicts that the decay time τ_{diff} in an intrinsic semiconductor continuously changes with carrier density. How exactly the decay time depends on the properties of the trap varies depending on the situation. A potentially quite relevant case of a high density of acceptor-like traps close to the conduction band results in[55] $\tau_{diff} \approx \tau_p \sqrt{\frac{n_1 N_T}{np}} \frac{1}{1+k_{rad}\tau_p n_1} = \tau_p \frac{\sqrt{n_1 N_T}}{n_i} \frac{1}{1+k_{rad}\tau_p n_1} \exp(-\frac{\Delta E_F}{2kT})$, whereby τ_p is the hole lifetime, N_T is the trap density, $n_1 = N_C \exp(-(E_C - E_T)/kT)$ includes the trap-depth $E_C - E_T$, k_{rad} is the radiative recombination coefficient,

n is the electron density, p is the hole density, and N_C is the effective density of states of the conduction band. A similar equation can be derived for donor-like traps close to the valence band. The important aspect of these equations is that they deal with shallow traps that are uncharged in a situation of chemical equilibrium (dark, no applied voltage). These traps, therefore, start to become charged only in case of sufficient illumination or forward bias so that free carriers are injected into the conduction and valence bands. In this case, they lead to a decay time that is continuously changing with carrier density or Fermi-level splitting as previously observed in ref. [55]. Thus, we need to modify traditional approaches of[51,56,57] extracting the surface recombination velocity from the decay time by considering the carrier-density dependence of the decay time.

Then we can deduce the surface recombination velocity S from the differential decay time via

$$S\left(\Delta E_F\right) = 2d\left(\frac{1}{\tau_{diff}\left(\Delta E_F\right)} - \frac{1}{\tau_{bulk}\left(\Delta E_F\right)}\right) \tag{9}$$

The bulk recombination lifetime τ_{bulk} depends on the internal voltage. Given that our experimental data shows similar slopes as the ones predicted by the analytical model for shallow defects, it is a reasonable approach to express the bulk lifetime via $\tau_{bulk} = \tau_0 \exp(1.5\text{eV} - \Delta E_F)/(2kT)$. Here the slope is fixed but the absolute value is variable and determined by the parameter τ_0, which is defined such that it becomes equal to τ_{bulk} when $\Delta E_F = 1.5$ eV. As the bulk lifetime needs to be strictly larger than the measured decay time, we chose $\tau_0 = 1$ µs as indicated by the dark yellow dashed line in Figure 5c.

The surface-recombination velocity S versus ΔE_F then follows from Equation (9) and is shown in Figure 5d. Furthermore, S determined assuming different values of τ_0 is shown in Figure S18, Supporting Information. The samples with the longest decay time (Me-4PACz and Me-4PACz/PTAA) show a dependence of S on the assumed value of τ_{bulk}, while this assumption becomes irrelevant for the samples with lower decay times. The trend of S versus sample type is now the opposite of that of the measured decay time (longer decay times → lower values of S). It is noteworthy that S varies strongly with the Fermi level splitting which suggests that the interfacial defects are not in the middle of the interfacial band gap but are also shallow with respect to either of the two band edges.

2.6. Steady-State Photoluminescence

Steady-state photoluminescence (ss-PL) was carried out to investigate interfacial recombination at the different interfaces between the hole-transport layers and the perovskite absorber.[58,59] The structures of the samples used for ss-PL are glass/perovskite, glass/ITO/hole transport layers/perovskite, glass/ITO/ hole transport layers /perovskite/C_{60}, and the full device. The relative photoluminescence intensities as a function of laser intensities for glass/perovskite and ITO/hole transport layers/perovskite are summarized in Figure S19, Supporting Information. The quasi-Fermi level splitting ΔE_F of the layer stacks at 1 sun is shown in **Figure 6** and was calculated under the assumption of flat Fermi

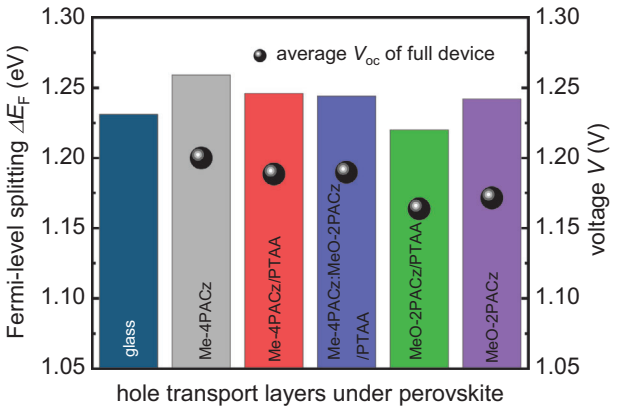

Figure 6. The calculated quasi-Fermi-level splitting of perovskite films deposited on different hole transport layers (bars) and average V_{oc} of cells with different hole transport layers (spheres).

levels at the open circuit from[50]

$$qV_{oc,imp}\left(\phi_{PL}\right) = qV_{oc}\left(\phi_{sun}\right) + kT\ln\left(\frac{\phi_{PL}}{\phi_{PL,cell}\left(\phi_{sun}\right)}\right) \tag{10}$$

where ϕ_{PL} is the photoluminescence of the samples shown in Figure 6. Here, $\phi_{PL,cell}(\phi_{sun})$ is the photoluminescence of the reference cell. The Me-4PACz/perovskite showed the highest quasi-Fermi level splitting of 1.259 eV. Consistent with the tr-PL results, SAM/PTAA/perovskite stacks lead to a reduction in quasi-Fermi level splitting compared to the SAM/perovskite stacks for a given SAM, suggesting more recombination at the PTAA-perovskite interface. The average value of the measured V_{oc} from full devices (black spheres in Figure 6) agrees well with the trend in the highest quasi-Fermi level splitting based on different hole transport layers. As shown in Figure S20, Supporting Information, after depositing C_{60} on top of the perovskite, there is an 84 meV reduction in quasi-Fermi level splitting, which can be ascribed to significant non-radiative recombination losses at the perovskite/C_{60} interface. Thus, while the perovskite/C_{60} interface causes a significant voltage loss decreasing V_{oc}, the effect is not strong enough to suppress the impact of the HTL/perovskite interfaces on the open-circuit voltage. As C_{60} is common to all devices investigated in the study, the HTL/perovskite interface is decisive in explaining the trends of V_{oc} with sample structure.

2.7. Voltage-Dependent Photoluminescence

Voltage-dependent PL provides an option to quantify recombination losses at any given voltage.[40,60–62] Thereby, it allows quantifying the relation between the slow extraction of charge carriers and recombination. This is an important and rare feature in solar cell characterization, as the majority of techniques quantifying recombination are used either on films, layer stacks, or devices at open circuits, where no charge-carrier extraction takes place. **Figure** 7a,b shows the quasi-Fermi level (ΔE_F) splitting versus the external voltage applied for the cells with different hole transport layers. Again, we assume $\Delta E_F\ (V_{oc}) = qV_{oc}$ at open circuit.

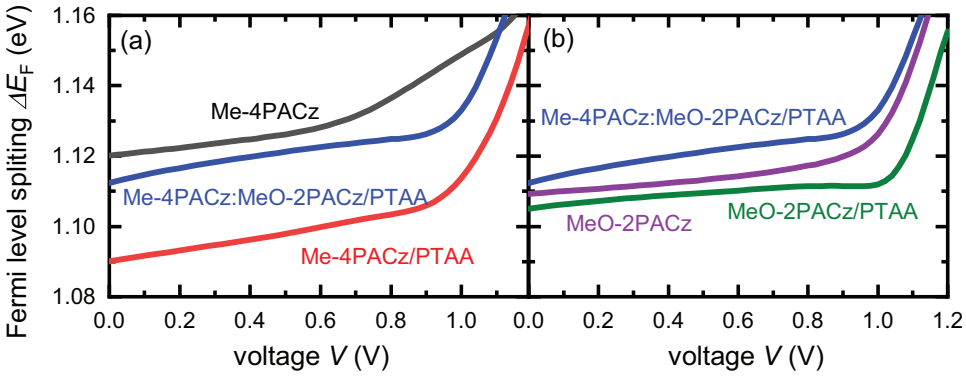

Figure 7. a,b) The quasi-Fermi level splitting determined from the voltage-dependent photoluminescence measurements as a function of the externally applied voltage for perovskite solar cells with different hole transport layers.

The quasi-Fermi level splitting at any applied voltage then follows from[50]

$$\Delta E_F(V) = kT \ln\left(\frac{\phi(V)}{\phi_{oc}}\right) + qV_{oc} \tag{11}$$

In an ideal scenario, the Fermi level is as high as possible at an open circuit and then drops to values as low as possible at a short circuit. In reality, however, there is still a quite significant Fermi-level splitting left that short circuit that indicates slow extraction of charge carriers. As this speed of extraction may be modified by the properties of the charge transport layers, we expect to see differences between the different hole-transport layers used.

The solar cells with Me-4PACz/PTAA and SAM mixture/PTAA have a lower ΔE_F than the cell with Me-4PACz at short-circuit and low forward voltage. The higher value of the quasi-Fermi level splitting at a short circuit implies a higher concentration of charge carriers remaining in the perovskite and thereby slow extraction.[31] In Figure 7b, the ΔE_F at short circuit of the cell with MeO-2PACz is higher than with MeO-2PACz/PTAA. But the SAM mixture /PTAA-bilayer shows a higher ΔE_F than both MeO-2PACz and MeO-2PACz/PTAA. According to the internal voltage as a function of the external voltage, the SAM/PTAA-based hole-transporting bilayers are more efficient in carrier extraction than the SAMs.

2.8. Influence of Charge-Carrier Extraction on Solar Cell Performance

As we have seen at the beginning of this article in Figure 1b, the efficiency of devices based on Me-4PACz decreases quite significantly as the perovskite film thickness increases. By depositing PTAA on top of the SAMs, the *FF* and J_{sc} of the micrometer-thick perovskite solar cells improved. We intuitively understand that the hole transport layer plays a critical role in the charge-carrier extraction processes and is thus influencing the *FF* and J_{sc} of solar cells. However, it is not immediately obvious why the hole-transport-layer properties should have such a strong impact on the thickness dependence of charge extraction. The traditional wisdom of solar cell device physics would predict that charge collection efficiencies depend on the ratio of diffusion or drift lengths on the absorber thickness.[34] However, diffusion and drift lengths account for transport in the absorber layer but not for transport in the charge-transport layers. Thus, a slightly different approach is required that explicitly considers a non-zero gradient of Fermi levels within the contact layers. This is equivalent to assuming that away from the open circuit, significant differences exist between the external voltage V_{ext} and the quasi-Fermi level splitting ΔE_F divided by elementary charge q, which is exactly what we have observed in the voltage-dependent PL measurements seen in Figure 7. If we assume that the most significant gradients in the Fermi level exist in the contact layers, the voltage-dependent current $J(V)$ can be determined by[63]

$$J(V_{ext}) = qd\left(R(V_{ext}) - G\right) = qd\left(\frac{1}{1 + d/\left(S_{exc}\tau_{eff}\right)}\right)\left(\frac{n_i}{\tau_{eff}}\left[\exp\left(\frac{qV_{ext}}{2kT}\right) - 1\right] - G\right) \tag{12}$$

where G is the average generation rate throughout the perovskite, $R(V)$ is the voltage-dependent recombination rate, n_i the intrinsic charge carrier concentration, τ_{eff} the effective carrier lifetime, and S_{exc} the exchange velocity. Equation (12) is a voltage-dependent version of similar equations previously derived for short circuits.[31,32] It is also a somewhat modified version of Equation (12) used in ref. [60] for explaining charge collection in $Cu(In,Ga)Se_2$ solar cells. An important and uncommon parameter in Equation (12) is the exchange velocity that describes how quickly charge carriers can be exchanged between electrode and absorber by drift and diffusion through the transport layer. Approximate equations for the exchange velocity exist for situations, where the electric field in the charge transport layer is approximately constant. In this case, we obtain[31,32,64] $S_{exc} = \mu_{CTL}F_{CTL}/(1 - \exp(U_{CTL}/kT))$, where μ_{CTL} is the mobility of charge carriers in the transport layers, F_{CTL} is the electric field in the charge transport layers, and U_{CTL} is the electrostatic potential drop (electric field times thickness). Equation (12) is based on the difference between recombination and generation currents, whereby both terms are multiplied with a prefactor $[1 + d/(S_{exc}\tau_{eff})]^{-1}$ that could be considered a collection efficiency. The ratio $d/(S_{exc}\tau_{eff})$ can be interpreted as the ratio of two lengths, namely the thickness d

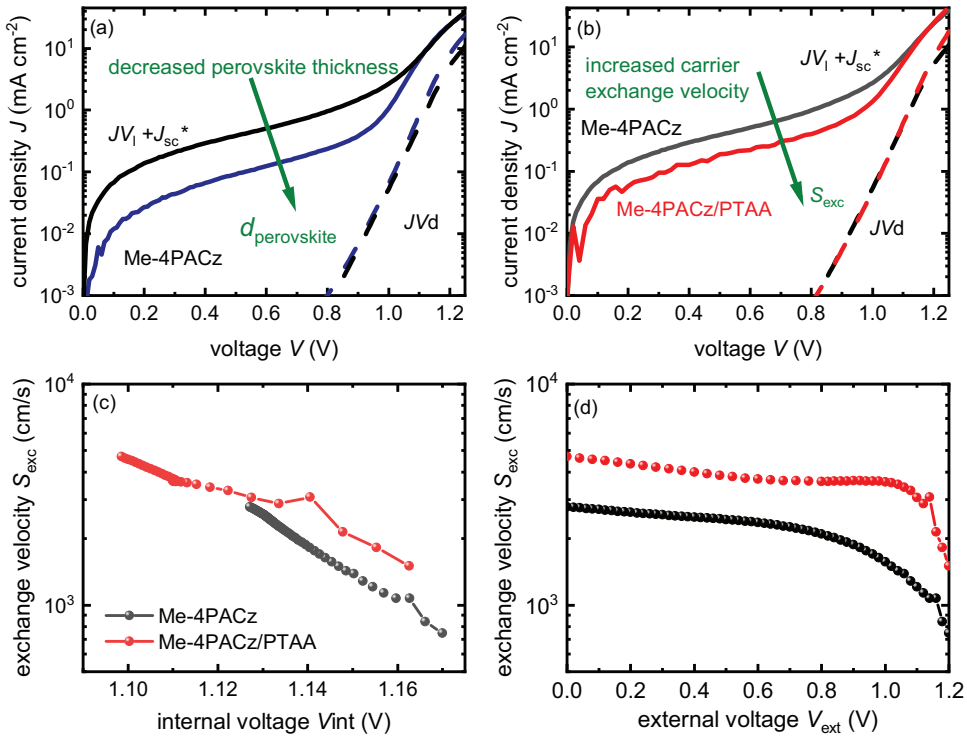

Figure 8. a) Dark (dashed line) and illuminated (solid line) *J–V* curve plotted in the first quadrant of perovskite solar cells with different thicknesses based on Me-4PACz. b) Dark (dashed line) and illuminated (solid line) *J–V* curve plotted in the first quadrant of perovskite solar cells with micrometer-thick perovskite solar cells with Me-4PACz and Me-4PACz/PTAA. Voltage dependence of the exchange velocity versus the internal voltage (c) and external voltage (d) of micrometer-thick perovskite solar cells with Me-4PACz and Me-4PACz/PTAA.

and a collection length $S_{exc}\tau_{eff}$ that contains the lifetime τ_{eff} of charge carriers in the absorber and the mobility and electric field of the charge carriers in the contact layer that enter the equation for S_{exc}. This ratio of lengths has the advantage of being conceptually analogous to the situation where the diffusion or drift length of the absorber limits charge collection. The ratio could also be interpreted as the ratio of two different time constants, whereby d/S_{exc} is a time constant for extraction and τ_{eff} is the time constant for recombination. In this interpretation, the ratio $d/(S_{exc}\tau_{eff})$ describes how much faster extraction is relative to recombination and is therefore an intuitive figure of merit for charge collection, which is also quite useful for the interpretation of time- or frequency-domain measurements.[63,65]

While there is an equation that allows relating S_{exc} to the mobility and electric field in the transport layers, this equation does not allow easy experimental access to the quantity. However, it is possible to express the difference in internal and external voltage as a function of the speed of exchange between the absorber and contact layers. This leads to an equation for the current density

$$J\left(V_{ext}, V_{int}\right) = qn_i S_{exc}\left(\exp\left(\frac{qV_{ext}}{2kT}\right) - \exp\left(\frac{qV_{int}}{2kT}\right)\right) \quad (13)$$

flowing into or out of the absorber layer that can be solved to obtain S_{exc}. Here, V_{ext} is the external voltage applied to the cells and V_{int} is the internal voltage (i.e., the average quasi-Fermi level splitting divided by elementary charge). While J and V_{ext} result from a normal measurement of the current–voltage curve under illumination, the missing parameter $q\,V_{int} = \Delta E_F$ can be obtained from the application of Equation (11) to voltage-dependent photoluminescence measurements as those previously shown in Figure 7. Thus, we have now presented a methodology for relating the result of the voltage-dependent PL measurements to the performance of the solar cells.

Figure 8a shows dark *J–V* curves and illuminated *J–V* curves of solar cells with different perovskite film thicknesses by using Me-4PACz as the hole transport layer that is shifted to the first quadrant by adding the respective J_{sc}. We note that the photoshunt-conductance increases with larger absorber thicknesses. The illuminated *J–V* curves shown in Figure 8a are the same as the ones shown in Figure 1b but plotted in a different way. In Figure 1b, we already learned that the J_{sc} and *FF* of thick cells with Me-4PACz are reduced relative to thin cells. Based on our knowledge and understanding of charge collection derived from Equation (12), we can now rationalize these observations. Equation (12) predicts that if the $\tau_{eff}S_{exc}$ product remains constant, the charge-collection losses will increase for larger thicknesses. This is a peculiar finding as it connects the poor mobility in the transport layers to the thickness of the absorber layer. Thus, even with infinite mobility of electrons and holes in the absorber layer, there might be non-zero and even substantial collection losses visible at short circuits or the MPP if the transport layers are poorly conductive and fairly intrinsic organic semiconductors. The slow transport through this layer will show up in three different ways throughout this paper: It shows up as a non-linear series resistance in Figure 3c, as a high quasi-Fermi level splitting at $V < V_{oc}$ in Figure 7 and

as a photoshunt in Figures 3a,b and 8a,b. Finally, this effect explains the lower efficiencies of solar cells with thicker perovskite absorber layers seen in Figure 1b.

Figure 8b shows the dark *J–V* curves and illuminated *J–V* curves of micrometer-thick perovskite solar cells with Me-4PACz and Me-4PACz/PTAA that are shifted to the first quadrant by adding the respective J_{sc}. The lower photoshunt conductance of the solar cell with a Me-4PACz/PTAA bilayer compared to the cell with a Me-4PACz monolayer is consistent with faster charge carrier extraction and visualizes again the advantage of the bilayer approach.

To further illustrate the better performance of micrometer-thick perovskite solar cells employing SAM/PTAA-bilayers as compared to solar cells using a single layer of SAMs, the voltage-dependent S_{exc} values of devices Me-4PACz and Me-4PACz/PTAA were calculated from Equation (13) and shown in Figure 8c,d. The solar cell with a Me-4PACz/PTAA bilayer has a higher exchange velocity S_{exc} than the cell with a single layer of Me-4PACz. The faster charge-carrier extraction speed, especially at short circuits, can explain the reason for the improved J_{sc} of devices with SAMs/PTAA-bilayers, as well as the lower series resistance leading to an improved *FF*.

3. Conclusions

An intermediate step to enable efficient, solution-processed perovskite top cells on textured Si bottom cells for tandem applications is the ability to design cell structures with suitably high band gaps (slightly below 1.7 eV) combined with high efficiencies at thickness above 1 µm. The main obstacle towards maintaining a high efficiency at higher thicknesses is currently a reduction in *FF* that is frequently observed when attempting to transfer recipes optimized for lower thicknesses to 1 µm-thick absorber layers. We observe that the optimization of the hole-transport layer offers an opportunity to maintain high *FF*s over a wide range of thicknesses. We achieve this by using a mixture of two SAMs—Me-4PACz and MeO-2PACz—which is subsequently covered by a thin layer of PTAA. Single-junction perovskite solar cells with an absorber thickness of around 1 µm and a bandgap of 1.68 eV reach fill factors of over 80% and efficiencies of around 20% when using such a hole-transporting bilayer.

The result that the effects of absorber-layer thickness can be mitigated by modifications of the charge-transport layers is initially counterintuitive as it defies the traditional logic of assigning thickness-dependent losses in solar cells to the mobility-lifetime product of the absorber layer. To better understand our loss-mitigation strategy, we performed an extensive characterization of resistive and recombination losses throughout the fourth quadrant of the current–voltage curve. A systematic analysis of illuminated current–voltage curve, dark current–voltage curve, and $J_{sc}V_{oc}$ measurements under different light intensities allow us to quantify resistive losses that already reveal differences between different hole-transport layers. In particular, Me-4PACz leads to significant resistive losses that can partially be rationalized by it having by far the highest ionization potential, which is likely to create a barrier for hole extraction to our used perovskite absorber. Subsequently, we use steady-state and transient PL to quantify recombination losses at interfaces and in the bulk of our perovskite absorber. We observe that the trend in the Fermi-level splitting derived from steady-state PL intensity versus used HTL in glass/ITO/HTL/perovskite half cells corresponds to the trend in V_{oc} in complete cells, while the absolute values are significantly lower. The latter observation implies that significant voltage losses occur at the perovskite-C_{60} interface as has been frequently observed in the literature.[1,13,66,67] Transient PL data shows continuously changing decay times in half cells, which is a signature of shallow defects. We, therefore, modify the existing methods to determine surface-recombination velocities to account for this and obtain carrier-density-dependent surface-recombination velocities. This finding suggests that interfacial recombination occurs via localized states at the perovskite-HTL interface that are not in the middle of the interfacial gap but are significantly closer to one of the bands. Finally, we use voltage-dependent steady-state PL measurements to quantify the extraction efficiency of charge carriers using a recently introduced new figure of merit called exchange velocity S_{exc}. We show how to determine the exchange velocity and how it affects the current–voltage curve in a relatively simple analytical model (see Equation (12)). The analytical model predicts that for constant recombination lifetimes and constant exchange velocities, the efficiency of charge-carrier collection quite naturally deteriorates for increasing absorber thicknesses. Thus, even without invoking arguments about the mobility-lifetime product of the absorber layer, it is possible to explain how modifications of the properties of hole extraction can affect the thickness dependence of solar cell performance. The necessary improvement of HTL properties is implemented technologically by adding additional degrees of freedom into the process. We do this by using a combination of two layers and by using a blend of two molecules in one of the layers. As we can observe from UPS and our various optical characterization techniques, this technological strategy allows us to finely tune energy-level positions and electronic properties to maximize majority-carrier extraction and minimize recombination speed at the interface. The strategy thereby improves the selectivity of the contacts in such a way that it minimizes efficiency reductions for increased absorber-layer thicknesses.

Supporting Information

Supporting Information is available from the Wiley Online Library or from the author.

Acknowledgements

The authors acknowledge support from the Helmholtz Association via the projects Zeitenwende, SolarTap and the project-oriented funding (POF IV). The authors also acknowledge funding from the German Research Foundation (DFG) for the project CREATIVE within the SPP "Perovskite Semiconductors: From Fundamental Properties to Devices" (SPP 2196). Open access publication funded by the DFG – 491111487. Y.W. acknowledges the HITEC graduate school for a HITEC Fellowship.

Open access funding enabled and organized by Projekt DEAL.

Conflict of Interest

The authors declare no conflict of interest.

Data Availability Statement

The data that support the findings of this study are available from the corresponding author upon reasonable request.

Keywords

charge transport layers, non-radiative recombination, perovskite, photoluminescence, series resistance

Received: August 9, 2023
Revised: November 25, 2023
Published online: December 8, 2023

[1] Z. Li, B. Li, X. Wu, S. A. Sheppard, S. Zhang, D. Gao, N. J. Long, Z. Zhu, *Science* **2022**, *376*, 416.
[2] M. Cai, Y. Wu, H. Chen, X. Yang, Y. Qiang, L. Han, *Adv. Sci.* **2017**, *4*, 1600269.
[3] H. Min, D. Y. Lee, J. Kim, G. Kim, K. S. Lee, J. Kim, M. J. Paik, Y. K. Kim, K. S. Kim, M. G. Kim, T. J. Shin, S. Il Seok, *Nature* **2021**, *598*, 444.
[4] O. Almora, D. Baran, G. C. Bazan, C. I. Cabrera, S. Erten-Ela, K. Forberich, F. Guo, J. Hauch, A. W. Y. Ho-Baillie, T. J Jacobsson, R. A. J. Janssen, T. Kirchartz, N. Kopidakis, M. A. Loi, R. R. Lunt, X. Mathew, M. D. Mcgehee, J. Min, D. B. Mitzi, M. K. Nazeeruddin, J. Nelson, A. F. Nogueira, U. W. Paetzold, B. P. Rand, U. Rau, H. J. Snaith, E. Unger, L. Vaillant-Roca, C. Yang, H.-L. Yip, et al., *Adv. Energy Mater.* **2023**, *13*, 2203313.
[5] W. Shockley, H. J. Queisser, *J. Appl. Phys.* **1961**, *32*, 510.
[6] T. Kirchartz, U. Rau, *Adv. Energy Mater.* **2018**, *8*, 1703385.
[7] C. H. Henry, *J. Appl. Phys.* **1980**, *51*, 4494.
[8] A. Martí, G. L. Araújo, *Sol. Energy Mater. Sol. Cells* **1996**, *43*, 203.
[9] M. J. Keevers, M. A. Green, *Appl. Phys. Lett.* **1995**, *66*, 174.
[10] F. Sahli, J. Werner, B. A. Kamino, M. Bräuninger, R. Monnard, B. Paviet-Salomon, L. Barraud, L. Ding, J. J. Diaz Leon, D. Sacchetto, G. Cattaneo, M. Despeisse, M. Boccard, S. Nicolay, Q. Jeangros, B. Niesen, C. Ballif, *Nat. Mater.* **2018**, *17*, 820.
[11] Y. Hou, E. Aydin, M. De Bastiani, C. Xiao, F. H. Isikgor, D.-J. Xue, B. Chen, H. Chen, B. Bahrami, A. H. Chowdhury, A. Johnston, S.-W. Baek, Z. Huang, M. Wei, Y. Dong, J. Troughton, R. Jalmood, A. J. Mirabelli, T. G. Allen, E. Van Kerschaver, M. I. Saidaminov, D. Baran, Q. Qiao, K. Zhu, S. De Wolf, E. H. Sargent, *Science* **2020**, *367*, 1135.
[12] X. Li, W. Zhang, X. Guo, C. Lu, J. Wei, J. Fang, *Science* **2022**, *375*, 434.
[13] Q. Jiang, J. Tong, Y. Xian, R. A. Kerner, S. P. Dunfield, C. Xiao, R. A. Scheidt, D. Kuciauskas, X. Wang, M. P. Hautzinger, R. Tirawat, M. C. Beard, D. P. Fenning, J. J. Berry, B. W. Larson, Y. Yan, K. Zhu, *Nature* **2022**, *611*, 278.
[14] Q. Guo, C. Li, W. Qiao, S. Ma, F. Wang, B. Zhang, L. Hu, S. Dai, Z. Tan, *Energy Environ. Sci.* **2016**, *9*, 1486.
[15] D. Liu, M. K. Gangishetty, T. L. Kelly, *J. Mater. Chem. A* **2014**, *2*, 19873.
[16] R. Brendel, H. J. Queisser, *Sol. Energy Mater. Sol. Cells* **1993**, *29*, 397.
[17] T. Kirchartz, L. Krückemeier, E. L. Unger, *APL Mater.* **2018**, *6*, 100702.
[18] P. Kaienburg, U. Rau, T. Kirchartz, *Phys. Rev. Appl.* **2016**, *6*, 024001.
[19] B. Chen, S.-W. Baek, Y. Hou, E. Aydin, M. De Bastiani, B. Scheffel, A. Proppe, Z. Huang, M. Wei, Y.-K. Wang, E.-H. Jung, T. G. Allen, E. Van Kerschaver, F. P García De Arquer, M. I. Saidaminov, S. Hoogland, S. De Wolf, E. H. Sargent, *Nat. Commun.* **2020**, *11*, 1257.
[20] G. Yang, Z. Ni, Z. J. Yu, B. W. Larson, Z. Yu, B. Chen, A. Alasfour, X. Xiao, J. M. Luther, Z. C. Holman, J. Huang, *Nat. Photonics* **2022**, *16*, 588.
[21] X. Zheng, J. Liu, T. Liu, E. Aydin, M. Chen, W. Yan, M. De Bastiani, T. G. Allen, S. Yuan, A. R. Kirmani, K. N. Baustert, M. F. Salvador, B. Turedi, A. Y. Alsalloum, K. Almasabi, K. Kotsovos, I. Gereige, L.-S. Liao, J. M. Luther, K. R. Graham, O. F. Mohammed, S. De Wolf, O. M. Bakr, *ACS Energy Lett.* **2022**, *7*, 1987.
[22] X. He, J. Chen, X. Ren, L. Zhang, Y. Liu, J. Feng, J. Fang, K. Zhao, S. Liu, *Adv. Mater.* **2021**, *33*, 2100770.
[23] Z. Liu, L. Qiu, E. J. Juarez-Perez, Z. Hawash, T. Kim, Y. Jiang, Z. Wu, S. R. Raga, L. K. Ono, S. Liu, Y. Qi, *Nat. Commun.* **2018**, *9*, 3880.
[24] X. Zhang, H. Huang, X. Ling, J. Sun, X. Jiang, Y. Wang, D. Xue, L. Huang, L. Chi, J. Yuan, W. Ma, *Adv. Mater.* **2022**, *34*, 2105977.
[25] J. Chen, L. Zuo, Y. Zhang, X. Lian, W. Fu, J. Yan, J. Li, G. Wu, C.-Z. Li, H. Chen, *Adv. Energy Mater.* **2018**, *8*, 1800438.
[26] K. Yan, J. Chen, H. Ju, F. Ding, H. Chen, C.-Z. Li, *J. Mater. Chem. A* **2018**, *6*, 15495.
[27] G. Tong, D.-Y. Son, L. K. Ono, Y. Liu, Y. Hu, H. Zhang, A. Jamshaid, L. Qiu, Z. Liu, Y. Qi, *Adv. Energy Mater.* **2021**, *11*, 2003712.
[28] Z. Xiao, Q. Dong, C. Bi, Y. Shao, Y. Yuan, J. Huang, *Adv. Mater.* **2014**, *26*, 6503.
[29] M. De Bastiani, A. J. Mirabelli, Y. Hou, F. Gota, E. Aydin, T. G. Allen, J. Troughton, A. S. Subbiah, F. H. Isikgor, J. Liu, L. Xu, B. Chen, E. Van Kerschaver, D. Baran, B. Fraboni, M. F. Salvador, U. W. Paetzold, E. H. Sargent, S. De Wolf, *Nat. Energy* **2021**, *6*, 167.
[30] P. Kaienburg, L. Krückemeier, D. Lübke, J. Nelson, U. Rau, T. Kirchartz, *Phys. Rev. Res.* **2020**, *2*, 023109.
[31] S. Akel, A. Kulkarni, U. Rau, T. Kirchartz, *PRX Energy* **2023**, *2*, 013004.
[32] O. J. Sandberg, J. Kurpiers, M. Stolterfoht, D. Neher, P. Meredith, S. Shoaee, A. Armin, *Adv. Mater. Interfaces* **2020**, *7*, 2000041.
[33] N. D. Arora, S. G. Chamberlain, D. J. Roulston, *Appl. Phys. Lett.* **1980**, *37*, 325.
[34] R. S. Crandall, *J. Appl. Phys.* **1983**, *54*, 7176.
[35] M. A. Green, *Sol. Cells* **1982**, *7*, 337.
[36] F. A. Lindholm, J. G. Fossum, E. L. Burgess, *IEEE Trans. Electron Devices* **1979**, *26*, 165.
[37] S. J. Robinson, A. G. Aberle, M. A. Green, *J. Appl. Phys.* **1994**, *76*, 7920.
[38] C. G. Shuttle, R. Hamilton, B. C. O'regan, J. Nelson, J. R. Durrant, *Proc. Natl. Acad. Sci. U. S. A.* **2010**, *107*, 16448.
[39] O. Breitenstein, *IEEE J. Photovoltaics* **2014**, *4*, 899.
[40] D. Grabowski, Z. Liu, G. Schöpe, U. Rau, T. Kirchartz, *Sol. RRL* **2022**, *6*, 2200507.
[41] D. Lübke, P. Hartnagel, M. Hülsbeck, T. Kirchartz, *ACS Mater. Au* **2023**, *3*, 215.
[42] M. Wolf, H. Rauschenbach, *Adv. Energy Convers.* **1963**, *3*, 455.
[43] T. C. M. Müller, B. E. Pieters, U. Rau, T. Kirchartz, *J. Appl. Phys.* **2013**, *113*, 134503.
[44] N. Mundhaas, Z. J. Yu, K. A. Bush, H.-P. Wang, J. Häusele, S. Kavadiya, M. D. Mcgehee, Z. C. Holman, *Sol. RRL* **2019**, *3*, 1800378.
[45] A. G. Aberle, S. R. Wenham, M. A. Green, In Proceedings of the 23rd IEEE Photovoltaic Specialists Conference, IEEE, New York **1993**, 133.
[46] A. Al-Ashouri, E. Köhnen, B. Li, A. Magomedov, H. Hempel, P. Caprioglio, J. A. Márquez, A. B. Morales Vilches, E. Kasparavicius, J. A. Smith, N. Phung, D. Menzel, M. Grischek, L. Kegelmann, D. Skroblin, C. Gollwitzer, T. Malinauskas, M. Jost, G. Matic, B. Rech, R. Schlatmann, M. Topic, L. Korte, A. Abate, B. Stannowski, D. Neher, M. Stolterfoht, T. Unold, V. Getautis, S. Albrecht, *Science* **2020**, *370*, 1300.
[47] A. Al-Ashouri, A. Magomedov, M. Roß, M. Jošt, M. Talaikis, G. Chistiakova, T. Bertram, J. A. Márquez, E. Köhnen, E. Kasparavičius, S. Levcenco, L. Gil-Escrig, C. J. Hages, R. Schlatmann, B. Rech, T. Malinauskas, T. Unold, C. A. Kaufmann, L. Korte, G. Niaura, V. Getautis, S. Albrecht, *Energy Environ. Sci.* **2019**, *12*, 3356.
[48] J. Haddad, B. Krogmeier, B. Klingebiel, L. Krückemeier, S. Melhem, Z. Liu, J. Hüpkes, S. Mathur, T. Kirchartz, *Adv. Mater. Interfaces* **2020**, *7*, 2000366.
[49] T. Kirchartz, J. A. Márquez, M. Stolterfoht, T. Unold, *Adv. Energy Mater.* **2020**, *10*, 1904134.

[50] Z. Liu, L. Krückemeier, B. Krogmeier, B. Klingebiel, J. A. Márquez, S. Levcenko, S. Öz, S. Mathur, U. Rau, T. Unold, T. Kirchartz, *ACS Energy Lett.* **2018**, *4*, 110.
[51] Z. Liu, J. Siekmann, B. Klingebiel, U. Rau, T. Kirchartz, *Adv. Energy Mater.* **2021**, *11*, 2003386.
[52] L. Krückemeier, B. Krogmeier, Z. Liu, U. Rau, T. Kirchartz, *Adv. Energy Mater.* **2021**, *11*, 2003489.
[53] F. Peña-Camargo, J. Thiesbrummel, H. Hempel, A. Musiienko, V. M. Le Corre, J. Diekmann, J. Warby, T. Unold, F. Lang, D. Neher, M. Stolterfoht, *Appl. Phys. Rev.* **2022**, *9*, 021409.
[54] J. Siekmann, A. Kulkarni, S. Akel, B. Klingebiel, M. Saliba, U. Rau, T. Kirchartz, *Adv. Energy Mater.* **2023**, *13*, 2300448.
[55] Y. Yuan, G. Yan, C. Dreessen, T. Rudolph, M. Hülsbeck, B. Klingebiel, J. Ye, U. Rau, T. Kirchartz, *Nat. Mater.* **2023**, https://doi.org/10.1038/s41563-023-01771-2.
[56] J. Tong, Q. Jiang, A. J. Ferguson, A. F. Palmstrom, X. Wang, J. Hao, S. P. Dunfield, A. E. Louks, S. P. Harvey, C. Li, H. Lu, R. M. France, S. A. Johnson, F. Zhang, M. Yang, J. F. Geisz, M. D. Mcgehee, M. C. Beard, Y. Yan, D. Kuciauskas, J. J. Berry, K. Zhu, *Nat. Energy* **2022**, *7*, 642.
[57] J. Wang, W. Fu, S. Jariwala, I. Sinha, A. K.-Y. Jen, D. S. Ginger, *ACS Energy Lett.* **2018**, *4*, 222.
[58] M. Stolterfoht, P. Caprioglio, C. M. Wolff, J. A. Márquez, J. Nordmann, S. Zhang, D. Rothhardt, U. Hörmann, Y. Amir, A. Redinger, L. Kegelmann, F. Zu, S. Albrecht, N. Koch, T. Kirchartz, M. Saliba, T. Unold, D. Neher, *Energy Environ. Sci.* **2019**, *12*, 2778.
[59] V. Sarritzu, N. Sestu, D. Marongiu, X. Chang, S. Masi, A. Rizzo, S. Colella, F. Quochi, M. Saba, A. Mura, G. Bongiovanni, *Sci. Rep.* **2017**, *7*, 44629.
[60] U. Rau, V. Huhn, B. E. Pieters, *Phys. Rev. Appl.* **2020**, *14*, 014046.
[61] M. Stolterfoht, V. M. Le Corre, M. Feuerstein, P. Caprioglio, L. J. A Koster, D. Neher, *ACS Energy Lett.* **2019**, *4*, 2887.
[62] A. Dasgupta, S. Mahesh, P. Caprioglio, Y.-H. Lin, K.-A. Zaininger, R. D. J. Oliver, P. Holzhey, S. Zhou, M. M. Mccarthy, J. A. Smith, M. Frenzel, M. G Christoforo, J. M. Ball, B. Wenger, H. J. Snaith, *ACS Energy Lett.* **2022**, *7*, 2311.
[63] L. Krückemeier, Z. Liu, T. Kirchartz, U. Rau, *Adv. Mater.* **2023**, *35*, 2300872.
[64] S. Ravishankar, Z. Liu, U. Rau, T. Kirchartz, *PRX Energy* **2022**, *1*, 013003.
[65] S. Ravishankar, Z. Liu, Y. Wang, T. Kirchartz, U. Rau, *PRX Energy* **2023**, *2*, 033006.
[66] P. Caprioglio, J. A. Smith, R. D. J. Oliver, A. Dasgupta, S. Choudhary, M. D. Farrar, A. J. Ramadan, Y.-H. Lin, M. G Christoforo, J. M. Ball, J. Diekmann, J. Thiesbrummel, K.-A. Zaininger, X. Shen, M. B. Johnston, D. Neher, M. Stolterfoht, H. J. Snaith, *Nat. Commun.* **2023**, *14*, 932.
[67] F. Ye, S. Zhang, J. Warby, J. Wu, E. Gutierrez-Partida, F. Lang, S. Shah, E. Saglamkaya, B. Sun, F. Zu, S. Shoaee, H. Wang, B. Stiller, D. Neher, W.-H. Zhu, M. Stolterfoht, Y. Wu, *Nat. Commun.* **2022**, *13*, 7454.